Editors' Suggestion

Electron cloud buildup and impedance effects on beam dynamics in the Future Circular e^+e^- Collider and experimental characterization of thin TiZrV vacuum chamber coatings

E. Belli,* P. Costa Pinto, G. Rumolo, A. Sapountzis, T. Sinkovits, and M. Taborelli
CERN, 1217 Meyrin, Geneva, Switzerland

B. Spataro and M. Zobov
INFN - LNF, Frascati, 00044 Roma, Italy

G. Castorina and M. Migliorati
University of Rome 'La Sapienza' and INFN Sezione Roma1, 00185 Roma, Italy

(Received 19 July 2018; published 26 November 2018)

The Future Circular Collider FCC-ee is a study toward a high luminosity electron-positron collider with a centre-of-mass energy from 91 GeV to 365 GeV. Due to the beam parameters and pipe dimensions, collective effects and electron cloud can be very critical aspects for the machine and can represent the main limitations to its performance. An estimation of the electron cloud build up in the main machine components and an impedance model are required to analyze the induced instabilities and to find solutions for their mitigation. Special attention has been given to the resistive wall impedance associated with a layer of nonevaporable getter (NEG) coating on the vacuum chamber required for electron cloud mitigation. The studies presented in this paper will show that minimizing the thickness of this coating layer is mandatory to increase the single bunch instability thresholds in the proposed lepton collider at 45.6 GeV. For this reason, NEG thin films with thicknesses below 250 nm have been investigated by means of numerical simulations to minimize the resistive wall impedance. In parallel, an extensive measurement campaign was performed at CERN to characterize these thin films, with the purpose of finding the minimum effective thickness satisfying vacuum and electron cloud requirements.

DOI: 10.1103/PhysRevAccelBeams.21.111002

I. INTRODUCTION

Among the studies aiming to design post-LHC particle accelerators at CERN, the high luminosity electron-positron Future Circular Collider FCC-ee [1] is considered as a potential first step toward the 100 TeV hadron collider FCC-hh, in the same 97.75 km tunnel. The lepton collider is being designed to cover a beam energy range from 45.6 GeV to 182.5 GeV, thus allowing us to study the properties of the Higgs, W and Z bosons, and top quark pair production thresholds with unprecedented precision. Electron cloud and collective effects due to the electromagnetic fields generated by the interaction of the beam with the vacuum chamber represent a serious issue by producing instabilities that can limit the machine operation and performance. An estimation of the multipacting thresholds for the electron cloud build up and an evaluation of the heat load in the main components of the positron ring will be presented in Sec. II, together with possible mitigation strategies. An impedance model is also needed to study the single bunch instabilities, to predict their effects on beam dynamics and to identify possible mitigation techniques. In general, in order to build the impedance model of an accelerator in its design stage, the impedance of each vacuum chamber component has to be characterized and minimized. This paper will present the contributions of specific machine components to the total impedance budget and their effects on the stability of the beam. In particular, Sec. III focuses on the resistive wall impedance of a Non-Evaporable Getter (NEG) coating which is required to reduce the secondary electron yield (SEY) of the surface for electron cloud mitigation and to improve vacuum conditions during operation. In the proposed lepton collider on the Z resonance, minimizing the thickness of this coating layer is mandatory to increase the single bunch instability thresholds in both transverse and longitudinal planes. However, reducing the thickness of NEG coatings can

*eleonora.belli@cern.ch
Also at University of Rome 'La Sapienza' and INFN Sezione Roma1, 00185 Roma, Italy.

TABLE I. FCC-ee baseline beam parameters used for beam dynamics and electron cloud studies.

Beam energy [GeV]	45.6
Circumference C [km]	97.75
Number of bunches/beam N_b	16640
Bunch population N_p [10^{11}]	1.7
Beam current I [A]	1.39
RF frequency f_{RF} [MHz]	400
RF voltage V_{RF} [MV]	100
Energy loss per turn [GeV]	0.036
Momentum compaction α_c [10^{-5}]	1.48
Bunch length $\sigma_{z,SR}$[a]/$\sigma_{z,BS}$[b] [mm]	3.5/12.1
Energy spread $\sigma_{dp,SR}/\sigma_{dp,BS}$ [%]	0.038/0.132
Horizontal tune Q_x	269.138
Vertical tune Q_y	269.22
Synchrotron tune Q_s	0.025
Horizontal emittance ϵ_x [nm]	0.27
Vertical emittance ϵ_y [pm]	1.0

[a]Synchrotron radiation.
[b]Beamstrahlung.

affect the performance of the material itself and therefore the maximum SEY and related electron cloud mitigation. For this reason, an extensive measurement campaign was performed at CERN to characterize TiZrV thin films with thicknesses below 250 nm. Section IV presents the coating process, the activation performance investigated by surface analysis as well as the SEY of the thin NEG coatings. In Sec. V, other important sources of wakefields are presented, together with the longitudinal impedance budget and the effects of all these components on the single bunch beam dynamics. Concluding remarks will end the paper. Table I summarizes the main beam parameters on the Z resonance, including beamstrahlung (BS) parameters. In collision, the BS effect results in a higher energy spread which lengthens the bunches, thus increasing the single bunch instability thresholds, as will be discussed in the last section.

II. ELECTRON CLOUD STUDIES

An important limitation for the lepton collider is the electron cloud (EC) build up in the positron ring. In the FCC-ee case, primary electrons, produced by ionization of the residual gas in the beam pipe or by photoemission due to synchrotron radiation (SR), are attracted and accelerated by the positron beam up to energies of several hundreds of eV. When the electrons strike the chamber walls with these energies, they produce secondary electrons that in turn can be absorbed, reflected or accelerated again by the following positron bunch, thus producing an avalanche of electron multiplication. This accumulation of electrons can interact with the pipe walls, causing the heating of the vacuum chamber and degradation of vacuum and diagnostics, or with the beam itself, inducing transverse instabilities, emittance growth, tune shift and spread and beam losses. This section presents EC studies for the lepton collider at 45.6 GeV. The EC build up has been analyzed in the drift space and in all the magnets of the machine (dipoles and quadrupoles in the arcs and final focusing quadrupoles in the interaction region). The multipacting threshold has been evaluated for each component by scanning the SEY of the surface. Numerical simulations have been performed with the PyECLOUD [2,3] code to study bunch spacing effects on the build up. The bunch parameters used for simulations are listed in Table I.

A. Multipacting threshold and heat load

The arcs of FCC-ee are based on FODO cells, each of which contains two main dipoles with lengths of 23.44 and 21.94 m and twin-aperture focusing and defocusing quadrupoles with the same length of 3.1 m. Dipoles occupy 81.8% of the total length of the collider. In these studies, we use the realistic shape of the vacuum chamber, modelled as a circular pipe with 35 mm radius and two rectangular antechambers on both sides where SR absorbers will be installed. For the final focusing quadrupoles of the interaction region (IR) the beam pipe is circular with 15 mm radius for the QC1 quadrupole and 20 mm radius for the QC2 quadrupole. For the beam optics in the arcs and around the interaction point one can refer to [4]. PyECLOUD simulations have been performed for all the magnetic elements and drift sections of the ring. The EC build up in each element has been simulated by scanning the SEY for different bunch spacings and by assuming an initial uniform electron distribution in the vacuum chamber of $10^9\,\mathrm{e}^-/\mathrm{m}$. This initial uniform electron distribution represents the survival of electrons between trains or between turns. It can affect only the initial transient of the build up process, the dominant steady-state density being determined by beam parameters, chamber geometry and SEY. The assumed initial density has been therefore disregarded in the following computation of the heat load. The secondary emission model used in simulations is described in [3]. According to high order mode power loss computations [5], bunch spacing of 10 and 17.5 ns are not acceptable for the present cavity geometry and filling schemes with at least 100 rf buckets between the first bunches of consecutive trains are preferred. Therefore, for these studies we assume 4 trains of 80 bunches interleaved with 25 empty buckets by considering different bunch spacings of 2.5, 5, and 15 ns. The nominal bunch intensity of 1.7×10^{11} e^+/bunch has been used for all simulations. The magnetic parameters of each element are shown in Table II. Table III summarizes the multipacting threshold, defined as the highest SEY without multipacting, for each element and beam. These results show that the highest thresholds of EC multipacting are given by the 2.5 ns beam in the arcs and by the 15 ns beam in the IR. It is important to note that in the arcs the multipacting threshold is higher for shorter bunch spacing. This result should not be surprising since there are two extreme cases where multipacting does not occur: (i) in the case of continuous beam (or very small

TABLE II. Magnet parameters used for build up simulations at 45.6 GeV.

Element	Length [m]	Magnetic field
Arc dipole	23.44	0.01415 T
Arc quadrupole	3.1	±5.65 T/m
Arc drift	...	...
QC1L1	1.2	−96.3 T/m
QC1L2	1.0	50.3 T/m
QC1L3	1.0	9.8 T/m
QC2L1	1.25	6.7 T/m
QC2L2	1.25	3.2 T/m

TABLE III. Threshold SEY for multipacting for all the ring components.

Element	2.5 ns	5 ns	15 ns
Dipole	1.1	1.1	1.0
Quadrupole	1.2	1.0	<1.0
Drift	1.8	1.3	1.0
QC1L1	1.0	1.1	1.3
QC1L2	1.0	1.0	1.4
QC1L3	1.2	1.3	1.5
QC2L1	1.0	1.0	1.2
QC2L2	1.0	1.0	1.2

bunch spacing) where electrons remain trapped around the beam: when electrons are attracted and accelerated by a bunch, the next bunch could be closer enough to attract these electrons again before they reach the pipe walls, thus reducing the secondary emission. (ii) in the case of very large bunch spacing: electrons with low energy generated after the passage of a bunch are absorbed by the pipe walls before the arrival of the next bunch. The heat load has been calculated as the energy of electrons impacting the pipe walls over the simulated time range rescaled to the total beam intensity. As an example, Fig. 1 shows the evolution of the total number of electrons in the chamber of the FCC-ee arc dipoles as a function of time in case of 2.5 ns bunch

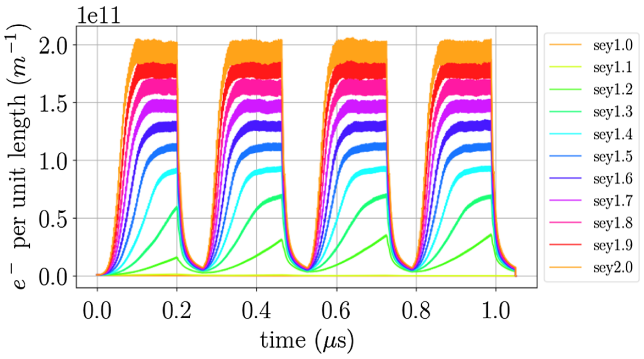

FIG. 1. Evolution of the total number of electrons in the chamber of the FCC-ee arc dipoles as a function of time in the case of 2.5 ns bunch spacing.

spacing. The initial transient visible only on the first simulated train has been excluded in the heat load computation, because it depends on the initial value of the electron density. Only trains where the electron distribution inside the chamber reaches a dynamic steady state have been considered. Figure 2 shows the EC induced heat load as a function of SEY for different components and bunch spacings. Numerical simulations have also been performed including photoemission seeding, modeled in PyECLOUD through photoelectron yield Y (quantum efficiency) and photon reflectivity R. Since in the case of FCC-ee with a critical photon energy of $E_c \simeq 19$ keV no experimental data exist for these parameters, we assume in build up simulations a photoelectron yield $Y = 0.02$ (similarly to the one considered for SuperKEKB studies [6]) and a reflectivity in the range $R = [30\%, 80\%]$. Results for arc dipoles in case of 15 ns bunch spacing are presented in Fig. 3, in case of uniform seeding (no photoelectrons) and for different values of reflectivity and photoelectrons, obtained by assuming that 50%, 75%, and 95% of photons are absorbed by the SR absorbers installed in the rectangular antechambers of the beam pipe. This plot shows that the heat load is not affected by photoelectrons: after an initial transient the build up and maintenance of the EC is mainly determined by the secondary emission, while the dependence on the photoemission parameters is marginal. Similar results have been obtained for arc quadrupoles and drifts.

B. Electron density threshold for transverse instability

EC single bunch head tail instability has been analyzed and observed in several machines [7,8]. This instability is produced by the interaction of the bunch with the EC: if the head of the bunch is slightly displaced from the beam axis when entering the EC, electrons will be attracted towards the head centroid position and there will be an EC formation in this region that will attract the following particles of the bunch. After a few passes through the EC, this will result in a strong deflection of the bunch tail. EC acts as a short range wake field with frequency

$$\omega_e = \sqrt{\frac{\lambda_p r_e c^2}{\sigma_y(\sigma_x + \sigma_y)}} \tag{1}$$

where $\lambda_p = \frac{N}{\sqrt{2\pi}\sigma_z}$ is the positron line density with N bunch population and σ_z bunch length, r_e is the classical electron radius and $\sigma_{x,y}$ are the transverse beam dimensions.

The threshold density for the instability is given by [8]

$$\rho_{th} = \frac{2\gamma Q_s \omega_e \sigma_z / c}{\sqrt{3} K Q r_e \beta_y C} \tag{2}$$

where Q_s is the synchrotron tune, C the machine circumference, $K = \omega_e \sigma_z / c$, $Q = \min(7, \frac{\omega_e \sigma_z}{c})$ and $\beta_y = \frac{C}{2\pi Q_y}$. Considering the baseline beam parameters of Table I, the

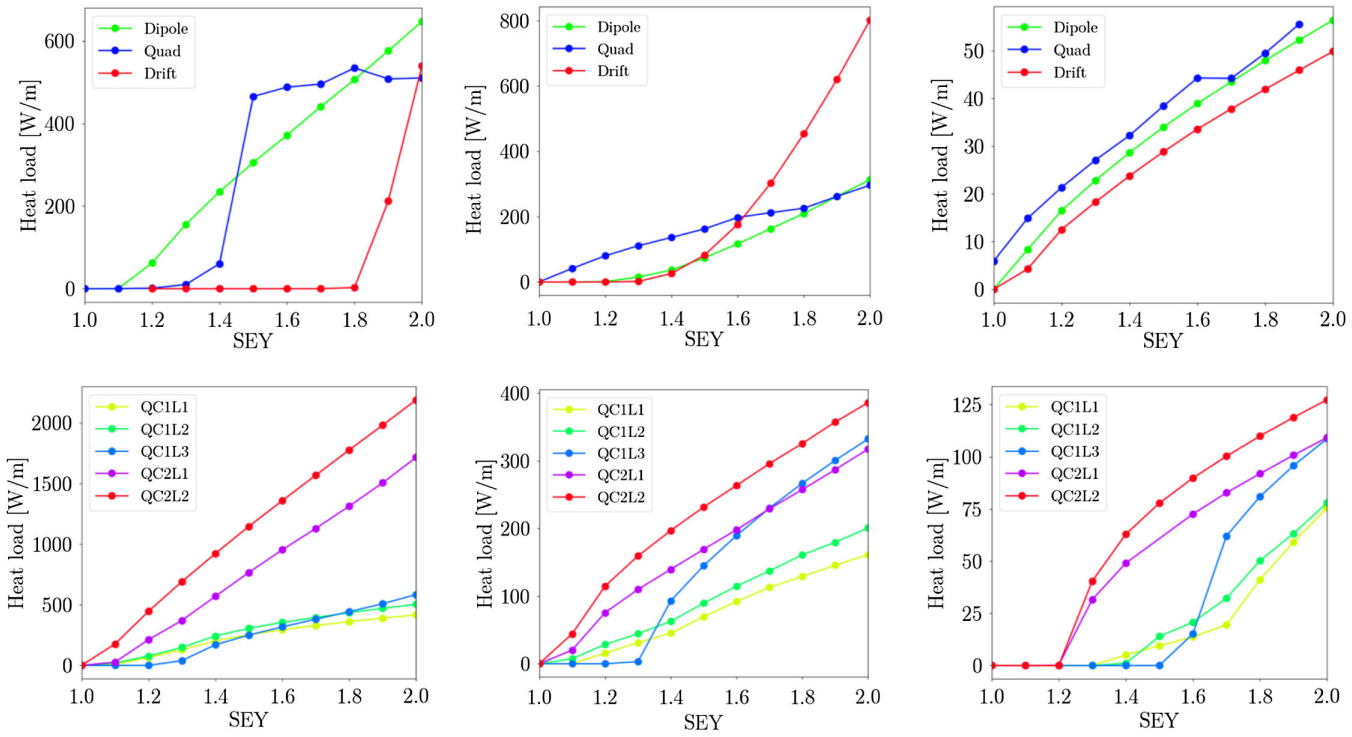

FIG. 2. Heat load as a function of SEY for arc components (top) and IR magnets (bottom) in the case of 2.5 ns (left side), 5 ns (center) and 15 ns (right side) bunch spacings.

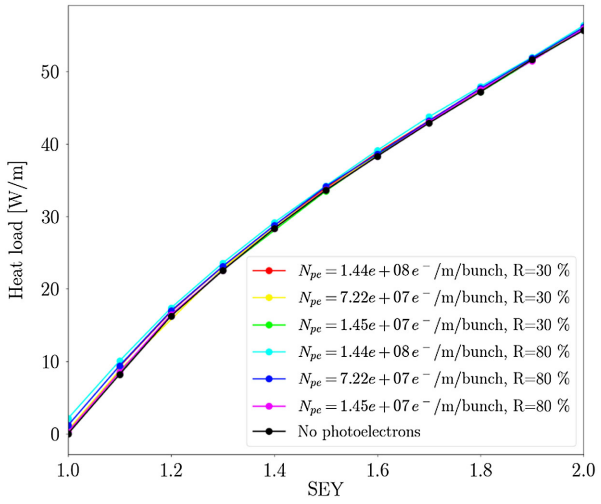

FIG. 3. Heat load as a function of SEY for arc dipoles in case of no photoelectrons and different values of photoelectrons and reflectivity.

corresponding electron density threshold for the transverse instability at low energy is about $2.29 \times 10^{10}/\mathrm{m}^3$. Such a low threshold can create potential problems for the collider operation and this issue requires further investigation by means of numerical simulations. Therefore, it is important to minimize the SEY in the entire ring by applying a low SEY coating, paying particular attention to the resistive wall impedance seen by the beam.

III. RESISTIVE WALL IMPEDANCE

Among the several sources of wakefields, a very critical contribution for the lepton machine design is the resistive wall (RW) impedance, produced by the finite conductivity of the pipe walls. This section focuses on the effects of the RW impedance on single bunch dynamics. For these studies, the vacuum chamber is assumed to be circular with 35 mm radius and three layers: a first inner layer of copper with 2 mm thickness, then 6 mm of dielectric to account for the gap between the beam pipe and the magnet chamber and finally the magnet chamber modeled as an outer layer of iron with resistivity $\rho = 10^{-7}$ Ωm and infinite thickness. For beam dynamics computations we consider as input the wakefields of this multilayer beam pipe obtained from the ImpedanceWake2D code [9,10]. However, considering that in the frequency range of interest of the lepton collider the electromagnetic fields do not penetrate beyond the copper layer, the following simplified analytic model will refer to a two-layer beam pipe. As already mentioned, a coating of the copper surface is foreseen to reduce the SEY of the chamber walls for the mitigation of the electron cloud build up in the machine and to optimise the vacuum environment during operation. On the basis of the positive experience of the Large Hadron Collider (LHC) warm sections [11,12], it was decided to use Ti-Zr-V NEG films to provide a surface with low photon-stimulated desorption (PSD) and SEY [13]. Previous studies on single bunch dynamics [14] pointed

out that in the case of FCC-ee the typical NEG film thickness of 1 μm makes the RW impedance responsible for quite low single bunch instability thresholds, in both transverse and longitudinal planes. It has been demonstrated [15] that under certain assumptions the longitudinal and transverse impedances of a two-layer beam pipe are given by the sum of two terms, one representing the impedance of a single layer pipe and a second term representing an inductive perturbation proportional to the thickness Δ of the coating:

$$\frac{Z_{\parallel}(\omega)}{C} \simeq \frac{Z_0 \omega}{4\pi c b}\left\{[\mathrm{sgn}(\omega) - i]\delta_2 - 2i\Delta\left(1 - \frac{\sigma_1}{\sigma_2}\right)\right\} \quad (3)$$

$$\frac{Z_{\perp}(\omega)}{C} \simeq \frac{Z_0}{2\pi b^3}\left\{[1 - i\mathrm{sgn}(\omega)]\delta_2 - 2i\Delta\mathrm{sgn}(\omega)\left(1 - \frac{\sigma_1}{\sigma_2}\right)\right\} \quad (4)$$

where Z_0 is the vacuum impedance, c the speed of light, b the pipe radius, σ_1 the conductivity of the coating layer and δ_2, σ_2 the skin depth and conductivity of the substrate, respectively. If the skin depth of the coating layer is much larger than its thickness and if the conductivity of the coating is much smaller than the conductivity of the substrate (conditions always verified in the FCC-ee case, also taking into account the variation of the NEG resistivity with frequency [16]), then the second term in Eqs. (3) and (4) becomes independent of the material conductivity and the effects of the impedances on the single bunch dynamics are affected mainly by the thickness of the coating layer. It follows that, for the beam parameters considered for the lepton collider at low energy, the contribution of the RW impedance can be reduced by decreasing the thickness of the coating. For this reason, the effects of NEG films with thicknesses below 250 nm on the single bunch beam dynamics have been studied by means of numerical simulations. In parallel these same thicknesses have been investigated experimentally, in order to find the minimum effective thickness ensuring a good activation performance for low PSD and SEY. This section is focused on impedance requirements and shows the effect on single bunch dynamics of reducing the thickness of NEG coatings.

A. Impact of NEG thickness

The most important effects of the RW impedance on the single bunch beam dynamics are the microwave instability (MI) in the longitudinal plane and the transverse mode coupling instability (TMCI) in the transverse plane [17]. Numerical simulations have been performed to study the impact of the thickness of the coating layer on the single bunch instability thresholds. NEG thin films at four different thicknesses of 1000, 200, 100, and 50 nm have been considered, with the beam parameters listed in Table I. Macro-particle beam dynamics has been simulated by using the tracking code PyHEADTAIL [18] developed at CERN to study a wide range of collective effects in synchrotrons. Systematic studies have been performed as comparisons with theoretical predictions and other simulation codes (SBSC, MuSiC, and BLonD described in [19–21], all of them benchmarked against theoretical and experimental data [22–24]). The excellent agreement found in all these comparisons increased the confidence in PyHEADTAIL results. PyHEADTAIL benchmark concerning TMCI threshold can be found in [25,26].

1. Longitudinal dynamics

The wake potential in PyHEADTAIL is computed as the convolution between the longitudinal wake function $w_{\parallel}(z)$ of a point charge and the bunch distribution $\lambda(z)$ [15]:

$$W_{\parallel}(z) = \int_{-\infty}^{z} w_{\parallel}(z - z')\lambda(z')dz' \quad (5)$$

For these studies, the wake potential of a very short Gaussian bunch with a bunch length $\sigma_z = 0.4$ mm has been used as the Green function for the code. The rationale behind this choice has been explained in [15]. Figure 4 shows the bunch lengthening and the energy spread

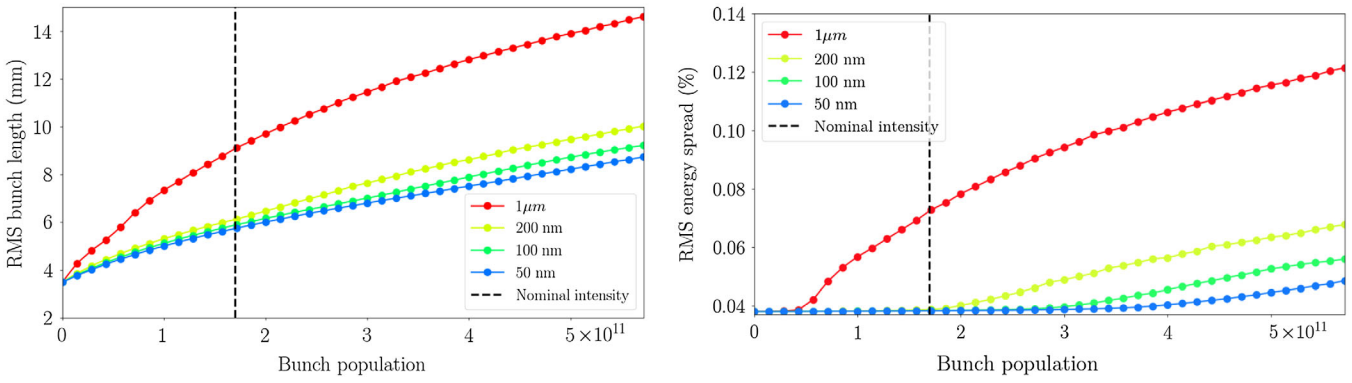

FIG. 4. RMS bunch length (left side) and RMS energy spread (right side) as a function of the bunch population given by numerical simulations considering only the RW impedance produced by NEG films with different thicknesses. The dashed black line corresponds to the nominal bunch population.

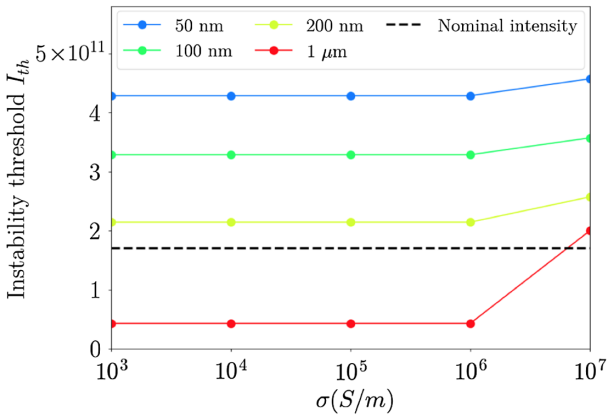

FIG. 5. MI threshold as a function of the coating conductivity for all thicknesses under study. The black dashed line corresponds to the nominal bunch intensity.

increase due to the longitudinal RW wakefield as a function of the bunch population for all the thicknesses under study. In these studies the instability threshold has been defined as the value of the bunch population corresponding to an increase of the energy spread of about 10% with respect to its nominal value. As already mentioned, a coating of 1 μm thickness makes the bunch unstable in the longitudinal plane, while thinner films allow to significantly increase the MI threshold. For example, in the case of 100 nm thickness the instability threshold is increased by a factor 7 with respect to 1 μm thickness and it is about 2 times higher than the nominal bunch intensity. Figure 5 shows the MI threshold as a function of the conductivity of the coating layer for all the considered thicknesses. This plot confirms what already stated for Eqs. (3) and (4): the threshold of the instability depends mainly on the thickness of the coating layer and only marginally on its conductivity.

2. *Transverse dynamics*

Another important effect of the transverse short range RW wakefield is the shift of the coherent betatron frequencies of the intrabunch modes when increasing the bunch intensity. The TMCI occurs when the frequencies of two modes are merging. For these studies, the TMCI threshold has been evaluated with the analytic Vlasov solver DELPHI [27] by taking into account bunch lengthening due to the longitudinal wake given by PyHEADTAIL at different intensities (see Fig. 4). Figure 6 shows the real part of the tune shift of the first two radial modes, with azimuthal number going from −2 to 2, as a function of the bunch population, for 100 nm and 1 μm thicknesses. For both thicknesses, the TMCI threshold is a factor of about 2.5 higher than the nominal bunch intensity. In the transverse case the thickness of the coating layer affects the threshold of the instability to a lesser extent than it does in the longitudinal plane. The longitudinal impedance produces longer bunches at higher intensities (see Fig. 4), which increases the TMCI threshold.

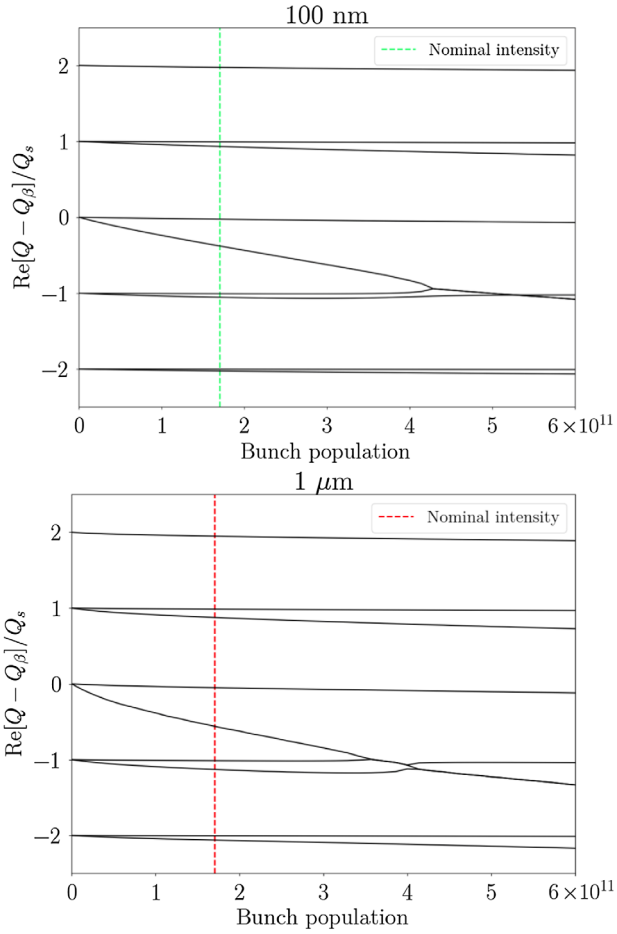

FIG. 6. Real part of the tune shift of the first coherent oscillation modes as a function of the bunch population for 100 nm (top) and 1 μm (bottom) thicknesses. The dashed lines represent the nominal bunch population.

IV. NEG THIN FILMS: EXPERIMENTAL RESULTS

In order to evaluate the activation performance and the SEY, NEG films at target thicknesses of 1000, 200, 100, and 50 nm were deposited on chemically polished copper samples by DC magnetron sputtering [28] in a cylindrical system. Intertwisted 3 mm diameter wires of Ti, Zr, and V were used as cathode and sputtered with a Kr working gas at a pressure of around 2.1×10^{-2} mbar. The stainless steel vacuum chamber was 95 mm in diameter and 1.5 m long, positioned in the centre of a solenoid providing a 200 G magnetic field. Samples were mounted at 46 mm from the cathode and a movable mask allowed deposition of coatings at different thickness in the same run. The relative atomic compositions of the film material were measured by energy dispersive x-ray spectroscopy to be 28% titanium, 29% zirconium and 43% vanadium. The thickness was measured on cross sections of the samples and determined by scanning electron microscopy (SEM) [29], resulting in film thicknesses of 1100, 203, 87, and 30 nm, obtained as average values from five measurements. Figure 7 shows the surface morphology of each sample: as seen by SEM, the

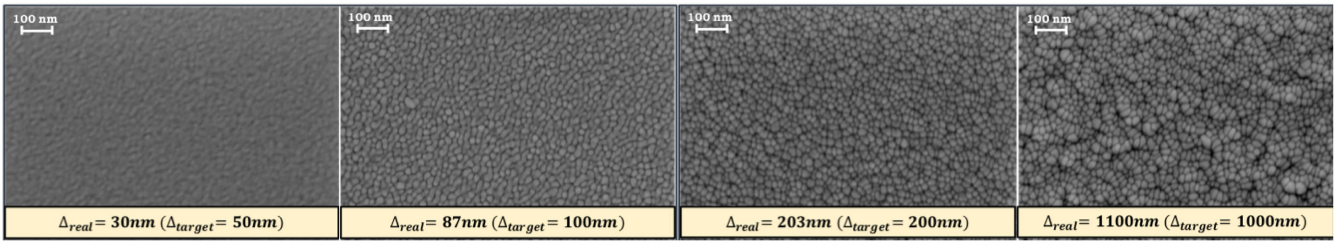

FIG. 7. Morphology of NEG thin films analyzed by SEM.

films cover the entire surface with a homogeneous thickness, while thicker films show an increasing roughness, the latter playing an important role on surface adsorption capacity and impedance.

A. Activation performance

The activation performance was measured by x-ray photoelectron spectroscopy (XPS) [30] by following changes to surface composition during a thermal treatment. The XPS spectra have been taken at four different steps for a total activation time of 4 hours: (i) as received sample, at room temperature (ii) after 1 hour heating at 160 °C (iii) after 1 hour heating at 200 °C (iv) after 1 hour heating at 250 °C.

This procedure of 4 steps will be referred to as a cycle in the following. This thermal activation was performed for 4 cycles, with air exposure between two consecutive cycles. The activation performance was evaluated by the reduction of the area of the oxygen peak O1s during a cycle of 4 hours. Figure 8 shows the O1s peak area as a function of the activation time and temperature after the fourth activation cycle: a higher reduction of the oxygen corresponds to a better activation and the plot shows that the oxygen surface concentration is increasing for thinner layers. XPS analysis also allowed observations of the oxidation state of the metals. The collected signals from Ti, Zr, and V on the uppermost surface of the films for activated states after the fourth activation cycle are shown in Fig. 9. The analysis of these photopeaks reveals the presence of mainly metallic

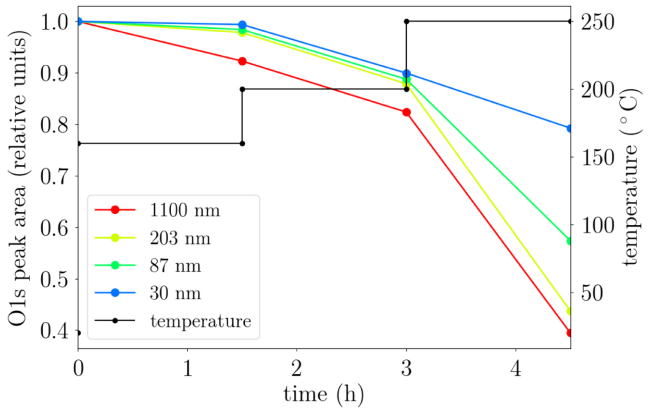

FIG. 8. Activation performance: reduction of the area of the oxygen peak from the XPS spectrum after the fourth activation cycle.

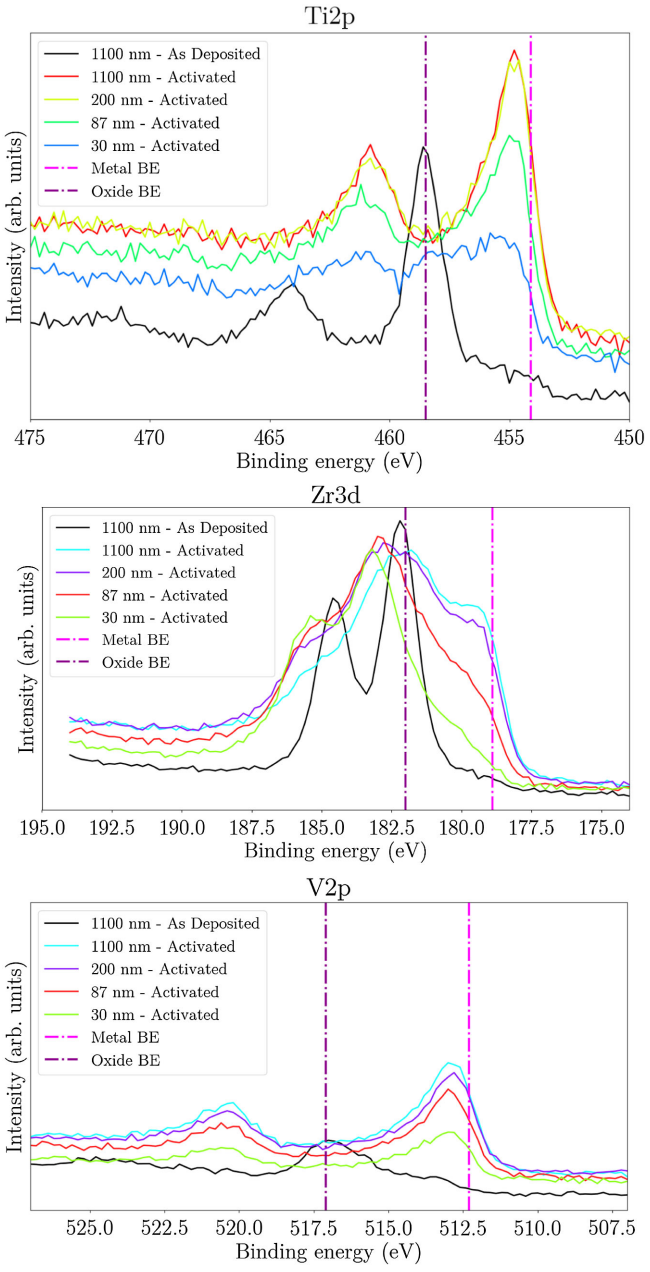

FIG. 9. Ti2p (top), Zr3d (center), and V2p (bottom) photopeaks obtained by XPS analysis for all the thicknesses under study. 2p and 3d refer to subshells of electronic configuration.

components on Ti and V while the Zr signal, which is the most sensitive in terms of activation due to its higher binding energy with oxygen, shows still a strong oxide component for the 87 and 30 nm films after activation.

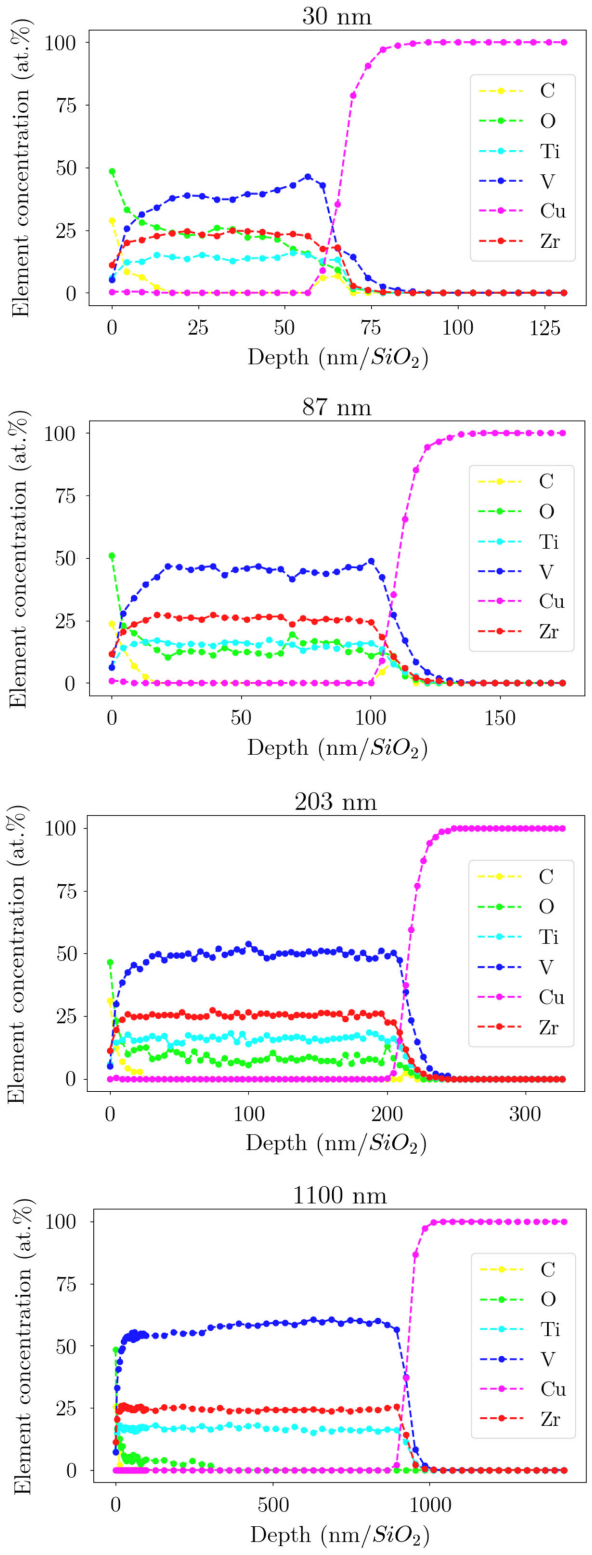

FIG. 10. Profile of C, O, Ti, V, Zr, and Cu as a function of depth for all the samples.

B. Depth profile

Figure 10 shows the depth profile, i.e., a XPS profiling of C, O, Ti, Zr, V and Cu from the surface of the layer to the Cu substrate, after the fourth activation cycle for each sample, in order to determine the elemental composition as a function of depth. The XPS profile was obtained by successive data acquisition and etching steps, performed using Ar^+ ions at 2 kV with an etching rate calibrated from a standard SiO_2 layer. This analysis shows that the oxygen content (green curve) is decreasing rapidly in all films but while in the 1100 nm sample it decreases below 5% in less than 100 nm, in the thinner samples it is detected in the whole layer, with the highest percentage close to 25% for the 30 nm film. As we will see in the next section, the presence of oxygen in the layer affects the activation performance and as a consequence the SEY. The migration of oxygen from the surface oxide to the bulk of the material is a diffusion process driven by concentration gradient, temperature and time and depending on the material structure (defining the availability of diffusion pathways). The diffusion of oxygen from high to low concentration zones will be faster in the case of a steep gradient, which is not the case of the 30 nm film, with an oxygen concentration going from 50% at the surface to 30% inside the layer. This represents a big loss in gradient and the major limiting factor, considering that the material structure is not changing at this activation temperature [31].

C. SEY measurements

SEY measurements were performed by using the apparatus shown in Fig. 11, consisting of an electron gun to produce primary electrons, a collector for emitted electrons and a holder with the samples under study. Primary electrons are accelerated in the electron gun to energies up to 1800 eV. All the SEY measurements reported in this paper have been carried out with a low primary electron current of about 5 nA and an angle of incidence normal to the surface of the sample. The beam was moved away from

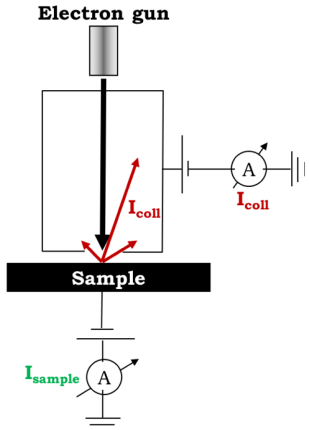

FIG. 11. SEY measurements apparatus.

the surface in between each measured point in order to avoid irradiation dose during the adjustment to the new primary energy. The dose cumulated during one full SEY curve is below 10^{-6} C/mm^2 to avoid any conditioning effect. A positive voltage (+45 V) is applied to the collector in order to capture all secondary electrons emitted by the sample and a negative bias (−18 V) is applied to the sample. The sample current I_{sample} and the secondary electron current I_{coll} are measured simultaneously by two current amplifiers with an accuracy of ±1% and the total SEY is computed as

$$\delta = \frac{I_{\text{coll}}}{I_{\text{coll}} + I_{\text{sample}}} \tag{6}$$

A reproducibility of ±3% can be considered for all the following SEY values. Figure 12 shows the SEY curves of NEG thin films for all the thicknesses under study after the fourth activation cycle. As already mentioned, for these studies samples were exposed to air between two consecutive activation cycles. The highest SEY of about 1.5 is obtained for the thinnest coating of 30 nm, due to incomplete activation, while the SEY value for a 87 nm coating is about 1.25 and is lower for thicker films. Elevated concentrations of oxygen in thinner films are responsible for higher SEY. In general, this is not a systematic effect, also when an oxide layer is created on the surface of the metal (see the case of copper exposed to

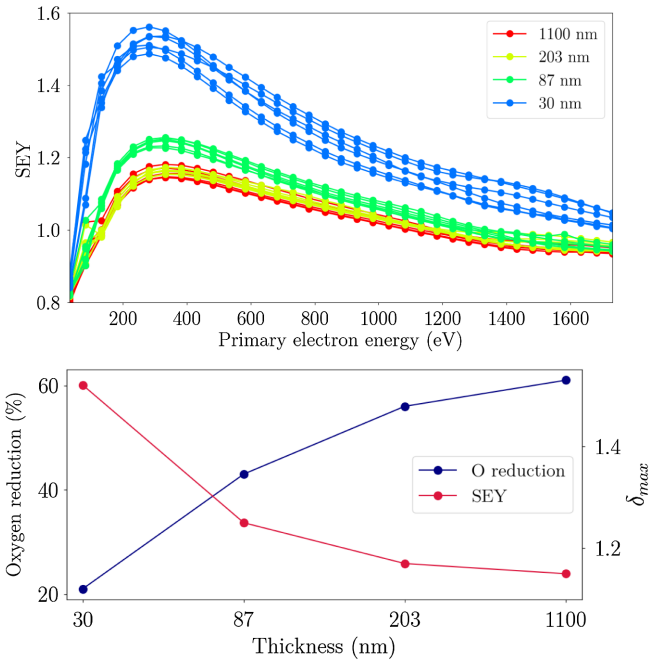

FIG. 12. SEY as a function of the photoelectrons energy (top) and oxygen reduction and maximum SEY as a function of the coating thickness (bottom) for all the samples under study after the fourth activation cycle of 4 hours up to a temperature of 250 °C.

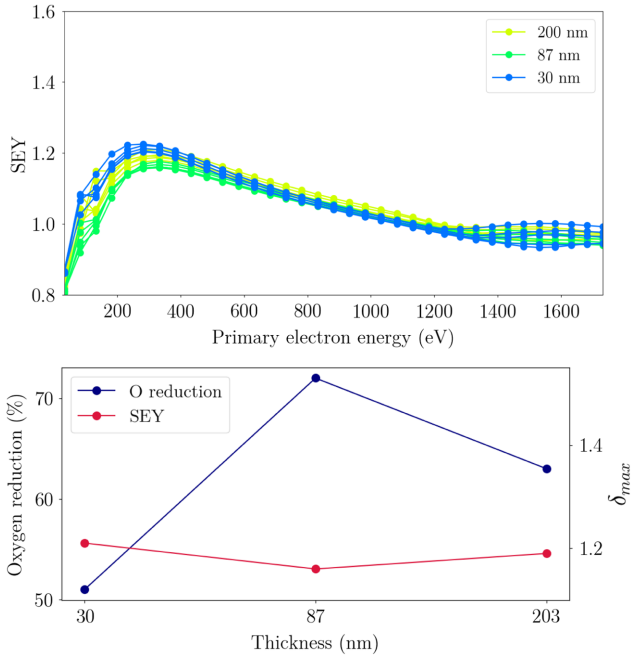

FIG. 13. SEY as a function of the photoelectrons energy (top) and oxygen reduction and maximum SEY as a function of the coating thickness (bottom) for the thin films after the fourth activation cycle of 24 hours up to a temperature of 250 °C.

pure oxygen [32]). However, in the case of Ti, Zr and V the increase of the SEY with oxygen is due to the building up of the oxides of these metals which have a higher SEY than the clean metal surface. These oxides are insulators or wide-band-gap semiconductors, meaning that secondary electrons which are excited can escape much easier from their surface provoking a higher SEY. Further SEY measurements have been performed after longer activation cycles of 24 hours at the same temperatures which are typical activation times for accelerator use. Observations after longer activation times show a lower SEY compared to the one obtained after shorter activation times, as shown in Fig. 13, where for example the maximum SEY for the 87 nm film was reduced from 1.25 to 1.16. These results confirm that activation is mainly a diffusion limited process: longer activation times allow oxygen at the film surface to migrate away and to lower the electron yield.

V. OTHER IMPEDANCE SOURCES

In addition to the RW impedance, there are other sources of wakefields in the machine that will be described in this section.

A. rf cavities and tapers

For the Z case, the rf system consists of about 56 cavities at 400 MHz with a single cell that will be arranged in groups of 4 cavities and connected by 14 double tapers (see Fig. 14). The number and the design of these cells have

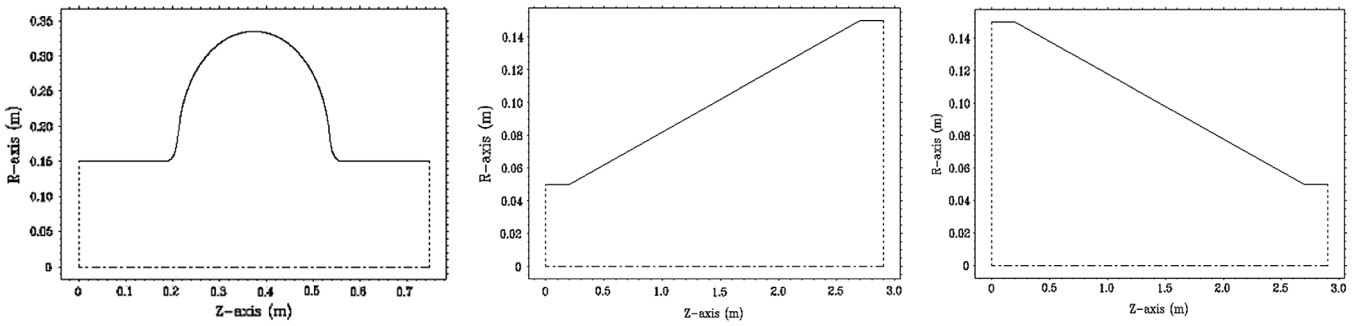

FIG. 14. 400 MHz single cell cavity and tapers used in ABCI.

been optimized for strong high order mode damping and low longitudinal loss factor [33,34]. For a Gaussian bunch with a nominal RMS bunch length of 3.5 mm, wakefield simulations with the ABCI code [35] estimated a loss factor of 0.33 V/pC for each cavity. By taking into account the 0.5 m long tapers used to connect the cavities with the beam pipe, we have an additional loss factor of 1.9 V/pC for a single double taper (in and out, considered independently). In total, the loss factor for 14 4-cell cavities at 400 MHz with double tapers will be 45.1 V/pC.

B. Synchrotron radiation absorbers

SR represents an important source of heating and photoelectrons for the machine. In order to recover the lost energy, a sufficient number of rf cavities is needed together with SR absorbers to cope with extra heating and eventual background. Due to their large number, SR absorbers may represent a very important source of wakefields. In order to reduce their contribution to the machine impedance budget, it was decided to use a circular vacuum chamber with 35 mm radius and two rectangular antechambers on both sides, as in the case of the SuperKEKB beam pipe [36]. Absorbers will be installed inside the chamber winglets every 4–6 meters, with the purpose of intercepting the radiation that, otherwise, would impact on the beam chamber. These metallic devices are trapezoidal shaped, with a total length of 30 cm and placed at about 42.5 mm from the beam axis, as shown in Fig. 15. Placing slots for vacuum pumps opposite each absorber allows to efficiently capture the molecule desorption. The pumping slots have a racetrack profile, length of 100–120 mm and width of 4–6 mm. Behind the slots, a cylindrical volume and a flange will be installed to support a NEG pump. CST [37] numerical simulations have been performed using the beam chamber profile with one absorber insertion. These impedance studies do not include pumping slots and pumps. Simulations show that below 3 GHz the longitudinal impedance is purely inductive, giving a longitudinal broadband impedance $Z_{\parallel}(n\omega_0)/n$, evaluated at the nth harmonic of the revolution frequency ω_0, of about 1 mΩ for 10000 absorbers in the ring.

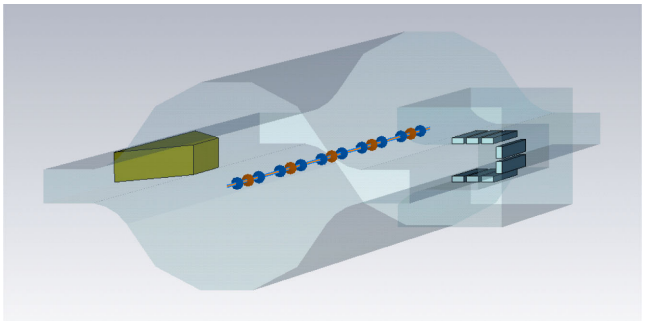

FIG. 15. CST 3D model of the FCC-ee chamber and a SR absorber with pumping slots.

C. Collimators

In order to suppress the background and to cut off the beam halo, a total number of 20 collimators (10 for each plane) are considered in this model, with a design very similar to those of PEP-II [38] and SuperKEKB [39]. 3D models used for CST simulations are shown in Fig. 16. By considering the minimum apertures of 5 and 2 mm for horizontal and vertical collimators, respectively, the total loss factor is about 18.7 V/pC for the nominal RMS bunch length of 3.5 mm.

D. Beam position monitors

Diagnostic elements like four-button beam position monitors (BPMs) are planned to be installed in the machine, for a total number of about 4000. In order to avoid special type of winglet-to-circular tapers, these elements will be installed directly on the beam pipe with a rotation angle of 45°. The geometry has been optimized from an impedance and heat transfer point of view [40]: the button has a diameter of 15 mm and a thickness of 3 mm. Moreover, in order to push the higher order modes trapped in the BPM structure to higher frequencies, a BPM design with a conical button, similar to the one used in SIRIUS [41], is also being considered (see Fig. 17). CST simulations in time domain have been performed and the total loss factor is about 40.1 V/pC for 4000 elements in the ring.

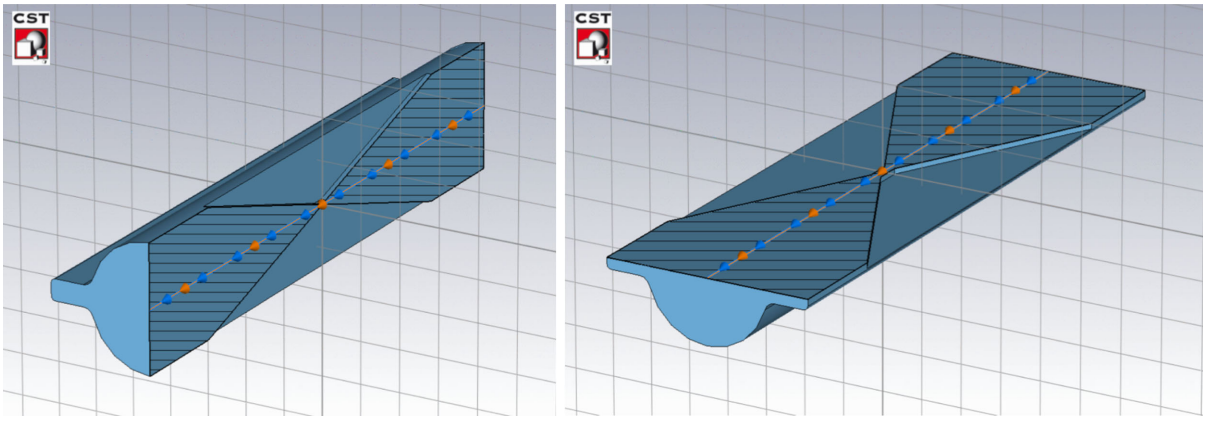

FIG. 16. CST perspective view of the vertical collimator (left side) and top view of the horizontal one (right side).

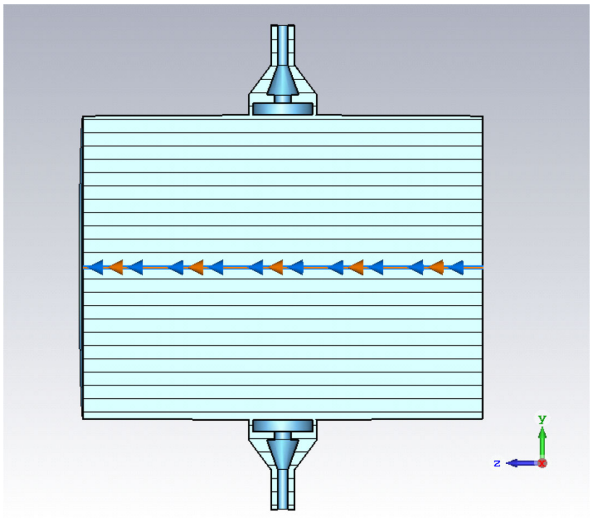

FIG. 17. Longitudinal cut of the four-button BPM model used in CST.

E. rf shielding

In addition to the previous components, bellows with rf shields will be installed before and after each BPM, for a total number of 8000. Since the conventional finger-type rf shielding showed a non-negligible impedance contribution compared to the RW impedance [42], it was decided to use comb-type bellows and flanges similar to those of SuperKEKB [43]. A 3D model was built using the CST code (see Fig. 18). In this case, the rf shielding consists of nested teeth with 10 mm length, 1 mm width, 0.5 mm radial thickness and 2.14 mm gap between adjacent teeth, corresponding to a gap of 0.57 mm between the nested teeth. This design also includes small fingers to ensure electrical contacts. The total loss factor of the bellows has been computed using CST and found to be about 49 V/pC for 8000 elements.

F. Longitudinal impedance model

The contribution of all the current machine components to the longitudinal impedance budget has been evaluated by means of ABCI and CST simulations in time domain for a Gaussian bunch with nominal RMS bunch length of $\sigma_z = 3.5$ mm. Figure 19 shows the longitudinal wake potentials of each component: from this plot it is evident that the other vacuum chamber components have a smaller impact on the impedance (and as a consequence on the beam dynamics) than does the RW. Table IV summarizes the corresponding loss factors. The major contribution to

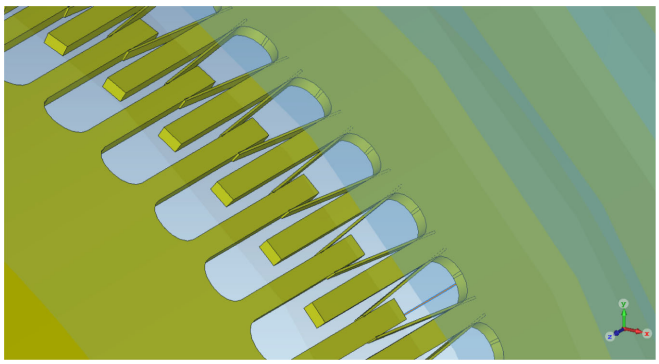

FIG. 18. Inside view of the rf shielding with small fingers between the teeth.

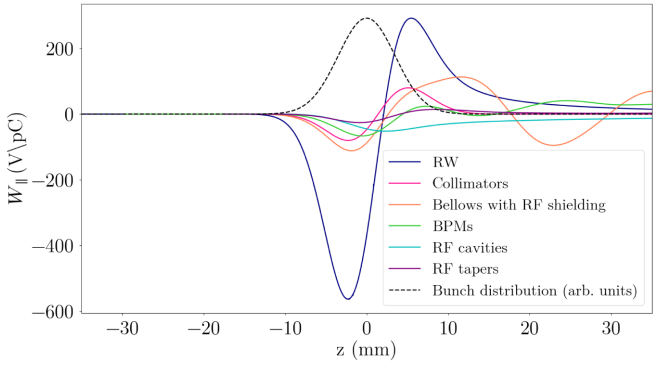

FIG. 19. Longitudinal wake potentials for a Gaussian bunch with nominal bunch length $\sigma_z = 3.5$ mm due to the main FCC-ee components compared with the RW contribution (blue line).

TABLE IV. Power loss contribution of the main FCC-ee components at nominal intensity and bunch length, in the lowest energy case of 45.6 GeV.

Component	Number	k_{loss}[V/pC]	P_{loss}[MW]
Resistive wall	97.75 km	210	7.95
Collimators	20	18.7	0.7
RF cavities	56	18.5	0.7
RF double tapers	14	26.6	1.0
BPMs	4000	40.1	1.5
Bellows	8000	49.0	1.8
Total		362.9	13.7

the machine impedance is given by the RW with a total loss factor at nominal intensity and bunch length of 210 V/pC. The total dissipated power at nominal intensity is 13.7 MW, about a factor 3.6 smaller than the total SR power dissipated by the beam of 50 MW. However, this value of power loss is expected to be lower due to the bunch lenghtening effect. As for the RW studies, by using as Green function for the PyHEADTAIL code the wake potential of a bunch with $\sigma_z = 0.4$ mm, the bunch lengthening and the MI threshold have been evaluated by considering all the current machine components and a 100 nm NEG film. The instability threshold in the longitudinal plane is about 2.5×10^{11}, a factor of 1.5 larger than the nominal bunch intensity, and it is much higher with beamstrahlung, as shown in Fig. 20, where the energy spread remains constant at least up to 5×10^{11}. Moreover, at nominal intensity there is an increase of the bunch length of only 7% in case of beamstrahlung while without beamstrahlung the bunch length is twice the nominal value.

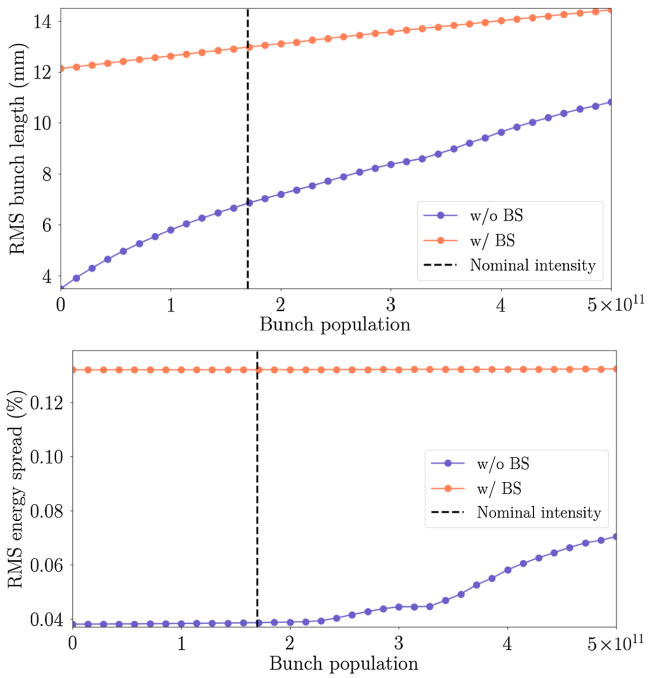

FIG. 20. RMS bunch length (top) and RMS energy spread (bottom) as a function of the bunch population with (orange curve) and without (blue curve) beamstrahlung (BS), given by numerical simulations by considering the impedance contribution of all the machine components.

VI. CONCLUSIONS

This paper presents the main limitations for the operation of the lepton collider FCC-ee. Electron cloud build up simulations have been performed for the main elements of the machine, in both the arcs and the interaction region. Multipacting thresholds and heat load have been evaluated for each component for bunch spacings 2.5, 5, 15 ns, indicating that with a low SEY coating the 15 ns beam is the preferable option to suppress the EC build up in the interaction region and to have a lower heat load in the arcs. In the case of EC induced head tail instability, further mitigation techniques must be investigated. The RW impedance represents the main source of wakefields in the machine and its contribution to the impedance budget can be reduced by decreasing the thickness of NEG coating needed for vacuum requirements and electron cloud mitigation. The minimum effective thickness for NEG activation was examined using XPS. The reduced activation performance is due to elevated concentrations of oxygen especially in the thinner films. The thinnest sample of 30 nm was able to digest O and C, however after four short activation cycles of 4 hours it was unable to activate effectively and this led to a high maximum SEY of 1.5. Longer activation cycles of 24 hours extended the effective lifetime of the 30 nm film, leading to better activation and a lower SEY of 1.21 after the fourth cycle. Numerical simulations and experimental results have indicated that a film thickness between 100 and 200 nm balancing the limitations of activation and impedance is a good candidate for coating thickness. Further experimental investigation is recommended for SEY and PSD with a larger number of activation cycles. Besides the RW, the geometric impedance has been evaluated for important machine components, showing that the contribution of these elements is up to 5 times smaller than that of RW. The MI threshold is around 2.5×10^{11}, about a factor 1.5 higher than the nominal bunch intensity. Operation with beamstrahlung, i.e., operation with colliding beams, will increase the instability thresholds in both planes, due to a larger bunch length and higher energy spread.

ACKNOWLEDGMENTS

The authors would like to thank D. Letant-Delrieux, H. Neupert, K. Oide, V. Petit, F. Zimmermann for their help and for the very useful discussions. This work was supported in part by the European Commission under the HORIZON 2020 Integrating Activity project ARIES, Grant Agreement No. 730871.

[1] http://tlep.web.cern.ch/.
[2] https://github.com/PyCOMPLETE/PyECLOUD.
[3] G. Iadarola, Electron cloud studies for CERN particle accelerators and simulation code development, CERN Report No. CERN-THESIS-2014-047, 2014.
[4] K. Oide, Status of optics, in *Proceedings FCC Week 2017, Berlin, Germany*, https://indico.cern.ch/event/556692/contributions/2590161/.
[5] I. Karpov, R. Calaga, and E. Shapochnikova, High order mode power loss evaluation in future circular electron-positron collider cavities, Phys. Rev. Accel. Beams **21**, 071001 (2018).
[6] H. Fukuma and L. F. Wang, Simulation study of the electron cloud instability in SuperKEKB, in *Proceedings of the 21st Particle Accelerator Conference, Knoxville, TN, 2005* (IEEE, Piscataway, NJ, 2005), p. 868.
[7] G. Rumolo, F. Ruggiero, and F. Zimmermann, Simulation of the electron-cloud build up and its consequences on heat load, beam stability, and diagnostics, Phys. Rev. ST Accel. Beams **4**, 012801 (2001).
[8] K. Ohmi, Study of electron cloud effects in SuperKEKB, in *Proceedings of IPAC'14, Dresden, Germany* (2014), p. 1597.
[9] N. Mounet, The LHC transverse coupled-bunch instability, CERN Report No. CERN-THESIS-2012-055, 2012.
[10] https://github.com/amorimd/CloneIW2D.
[11] P. C. Pinto, S. Calatroni, P. Chiggiato, H. Neupert, W. Vollenberg, E. Shaposhnikova, M. Taborelli, and C. Y. Vallgren, Thin film coatings for suppressing electron multipacting in particle accelerators, in *Proceedings of the 24th Particle Accelerator Conference, PAC-2011, New York, 2011* (IEEE, New York, 2011), p. 2096, https://cds.cern.ch/record/1462768.
[12] P. C. Pinto, History and potential of non evaporable getter (NEG) technology, in *Workshop on Advanced Materials and Surfaces, CERN, Geneva, Switzerland* (2013), https://indico.cern.ch/event/229108/contributions/1539894/.
[13] R. Kersevan, FCC-ee beam vacuum concept: The beam pipe of FCC-ee, in *Proceedings FCC Week 2018, Amsterdam, Netherlands*, https://indico.cern.ch/event/656491/contributions/2947258/.
[14] E. Belli, Impedance model and collective effects for FCC-ee, in *Proceedings FCC Week 2017, Berlin, Germany*, https://indico.cern.ch/event/556692/contributions/2590409/.
[15] M. Migliorati, E. Belli, and M. Zobov, Impact of the resistive wall impedance on beam dynamics in the Future Circular e^+e^- Collider, Phys. Rev. Accel. Beams **21**, 041001 (2018).
[16] E. Koukovini Platia, High frequency effects of impedances and coatings in the CLIC Damping Rings, CERN Report No. CERN-THESIS-2015-152.
[17] A. W. Chao, *Physics of collective beam instabilities in high energy accelerators* (Wiley, New York, 1993).
[18] https://github.com/PyCOMPLETE/PyHEADTAIL.
[19] M. Migliorati, S. Persichelli, H. Damerau, S. Gilardoni, S. Hancock, and L. Palumbo, Beam-wall interaction in the CERN Proton Synchrotron for the LHC upgrade, Phys. Rev. ST Accel. Beams **16**, 031001 (2013).
[20] M. Migliorati and L. Palumbo, Multibunch and multiparticle simulation code with an alternative approach to wakefield effects, Phys. Rev. ST Accel. Beams **18**, 031001 (2015).
[21] https://blond.web.cern.ch/.
[22] R. Boni, A. Drago, A. Gallo, A. Ghigo, F. Marcellini, M. Migliorati, F. Sannibale, M. Serio, A. Stella, G. Vignola, and M. Zobov, DAΦNE accumulator ring coupling impedance measurements, Nucl. Instrum. Methods Phys. Res., Sect. A **418**, 241 (1998).
[23] D. Quartullo, M. Migliorati, and J. Repond, Comparison of different methods to calculate induced voltage in longitudinal beam dynamics codes, in *Proceedings of IPAC'17, Copenhagen, Denmark* (2017), p. 4465, https://doi.org/10.18429/JACoW-IPAC2017-THPVA022.
[24] H. Timko, J. Esteban Müller, A. Lasheen, and D. Quartullo, Benchmarking the beam longitudinal dynamics code BLonD, in *Proceedings of IPAC'16, Busan, Korea* (2016), p. 3094, https://doi.org/10.18429/JACoW-IPAC2016-WEPOY045.
[25] H. Bartosik, Beam dynamics and optics studies for the LHC injectors upgrade, CERN Report No. CERN-THESIS-2013-257, 2013.
[26] E. Koukovini Platia, High frequency effects of impedances and coatings in the CLIC damping rings, CERN Report No. CERN-THESIS-2015-152, 2015.
[27] https://twiki.cern.ch/twiki/bin/view/ABPComputing/DELPHI.
[28] P. Chiggiato and P. Costa Pinto, Ti-Zr-V non-evaporable getter films: From development to large scale production for the Large Hadron Collider, Thin Solid Films **515**, 382 (2006).
[29] http://en-dep.web.cern.ch/en-dep/Groups/MME/MM/SEM.htm.
[30] J. F. Moulder *et al.*, Handbook of X-ray Photoelectron Spectroscopy, Perkin-Elmer Corporation, Physical Electronics Division, 1992.
[31] T. Sinkovits, Is NEG coating structure relevant for gas pumping?, in *TE-VSC Seminar, CERN, Geneva, Switzerland*, https://indico.cern.ch/event/628547/contributions/2538607/.
[32] C. Scheuerlein, The influence of an air exposure on the secondary electron yield of copper, CERN Report No. CERN-THESIS-2002-022, 2002.
[33] A. Butterworth, Cavity design and beam-cavity interaction challenges, in *Proceedings FCC Week 2017, Berlin, Germany*, https://indico.cern.ch/event/556692/contributions/2484361/.
[34] S. G. Zadeh, Cavity design approaches and HOM damping for FCC-ee, in *Proceedings FCC Week 2017, Berlin, Germany*, https://indico.cern.ch/event/556692/contributions/2484333/.
[35] http://abci.kek.jp/.
[36] Y. Suetsugu, K. I. Kanazawa, K. Shibata, T. Ishibashi, H. Hisamatsu, M. Shirai, and S. Terui, Design and construction of the SuperKEKB vacuum system, J. Vacuum Sci. Technol. A **30**, 031602 (2012).
[37] https://www.cst.com.
[38] S. DeBarger *et al.*, The PEP-II movable collimators, No. SLAC-PUB-11752, 2001.
[39] T. Ishibashi, Low impedance movable collimators for SuperKEKB, in *Proceedings of IPAC'17, Copenhagen,*

Denmark (2017), p. 2929, https://doi.org/10.18429/JACoW-IPAC2017-WEPIK009.

[40] F. Marcellini, M. Serio, A. Stella, and M. Zobov, DAPHNE broad-band button electrodes, Nucl. Instrum. Methods Phys. Res., Sect. A **402**, 27 (1998).

[41] A. Rodrigues *et al.*, Sirius status report, in *Proceedings of IPAC'16, Busan, Korea* (2016), p. 2811, https://doi.org/10.18429/JACoW-IPAC2016-WEPOW001.

[42] E. Belli, G. Castorina, M. Migliorati, A. Novokhatski, S. Persichelli, B. Spataro, and M. Zobov, Coupling impedances and collective effects for FCC-ee, in *Proceedings of IPAC'17, Copenhagen, Denmark* (2017), p. 3734, https://doi.org/10.18429/JACoW-IPAC2017-THPAB020.

[43] Y. Suetsugu, M. Shirai, and K. Shibata, Possibility of comb-type rf shield structure for high-current accelerators, Phys. Rev. ST Accel. Beams **6**, 103201 (2003).